Published in "Macromolecules 42(3): 849–859, 2009"
which should be cited to refer to this work.

Novel Phase Morphologies in a Microphase-Separated Dendritic Polymer Melt

Won Bo Lee,[†] Richard Elliott,[‡] Raffaele Mezzenga,[||,⊥] and Glenn H. Fredrickson*[,†,‡,§]

Department of Chemical Engineering, University of California, Santa Barbara, California 93106, Materials Research Laboratory, University of California, Santa Barbara, California 93106, Department of Materials, University of California, Santa Barbara, California 93106, Department of Physics, University of Fribourg, Perolles, Fribourg, CH-1700 Switzerland, and Nestle Research Center, Vers-Chez-Les-Blanc, 1000 Lausanne 26, Switzerland

ABSTRACT: Equilibrium phase morphologies of two different dendritic block copolymer melts are calculated and compared. These copolymers have a pitchfork-like architecture and consist of three distinct blocks that correspond roughly to the handle, the connecting middle dendron structure, and the attached tines of a pitchfork. The first melt considered consists of a copolymer that has a simple Y-junction middle block, and it connects the handle to two tines. The second is similar except its dendritic middle block branches twice to connect to four tines. Polymeric segments are modeled as flexible Gaussian threads and interactions between dissimilar blocks are all contact-like, Flory−Huggins repulsions. All calculations are done for incompressible melts in the context of self-consistent mean-field theory. We find that several morphologies compete for stability depending on the architecture and lengths of the blocks as well as their incompatibilities. As many as *four* stable two-dimensional phases appear in the phase diagram including: columnar square, rectangular and hexagonally packed structures. A long handle and a moderate length of the dendron are essential for stabilizing the square phases, and the four tine copolymer shows a larger region of stability for these phases compared to the Y-junction middle block system. A remarkable continuous phase transition between the square and rectangular phases is also found and investigated.

1. Introduction

A promising application of block copolymer self-assembly is in patterning lithographic templates. Substrates comprising thin films of microphase separated copolymers deposited on a nonreactive surface with one block subsequently removed, can provide templates for a variety microelectronic applications. They offer access to patterns on length scales less than 100 nm, which may be a straightforward and economical way of achieving nanostructures difficult to achieve with conventional optical lithography. Such "block copolymer lithography" utilizes the robust, in-plane assembly of block copolymers, and has shown potential in creating semiconductor devices and high density storage arrays.[1,2] Copolymer substrates can also be used as a substrate for photonic materials[3] and for fabrication of light-emitting displays.[4] Recent experimental and theoretical studies have shown that long-range order can be achieved in thin films of hexagonally packed, mesoscale domains by laterally confining the film in a well with the same boundary geometry.[5,6]

Although the self-assembly of linear block copolymers may be a reasonable way to engineer such nanoscale arrays, simple linear block copolymers have a limited number of stable two- and three-dimensional mesoscale structures. For example, the simplest system, an asymmetric AB diblock copolymer melt, has only one stable two-dimensional phase with discrete A and continuous B domains, namely the hexagonally packed cylinder phase.[7−10] Thin films of such diblocks assemble into an in-plane hexagonal lattice, which is less desirable than square lattices of microdomains in applications such as memory devices.

Block copolymers of different architectures, such as ABC triblock copolymers,[11] supramolecular blends of AB and B′C diblock copolymers,[12] T-shaped rod−coil chains[13−16] and dendronized polymers[17−20] form other, more desirable two-dimensional morphologies than the hexagonal lattice of the simple *AB* diblock. For example, T-shaped rod−coil polymers, such as those studied by Tschierske et al., assemble into several two-dimensional phases, and these include two cubic phases: square and rectangular packed cylinders, as well as the hexagonal phase. More complicated copolymer architectures, such as copolymeric dendrimers, also exhibit unusual morphologies, which include quasicrystalline and complicated three-dimensional cubic phases as well as a rectangular phase.[17,18,21] A recent study of supramolecular dendronized comblike polymers[22−25] indicates that this system has several thermodynamically stable, two-dimensional structures which include square, rectangular and hexagonal phases.

Until recently, theoretical studies that can provide molecular level insights for understanding phase morphologies in complex polymers have been largely unavailable due to the architectural complexity of these molecules. Although in principle simulations can be performed using an atomistic approach for these systems, the effectiveness of such an approach is generally very limited. The requisite number of atoms involved in structural assembly (greater than 10^6) and long simulation times (∼1 ms)[26−28] are prohibitive. For this reason, a statistical field theory approach based upon an underlying, coarse-grained model *that includes* architectural details, constitutes a significant advantage both from a physical and computational standpoint. This method, when solved in the mean-field or self-consistent field theory (SCFT) limit, also has a very successful track record for predicting equilibrium mesophase structures in flexible polymeric molecules under conditions where fluctuations do not sizably reduce the stability regions of the morphologies. In a recent investigation of a dendritic copolymer using this approach, the stability of a new cubic phase was demonstrated.[29,30]

* Corresponding author. E-mail: ghf@mrl.ucsb.edu.
[†] Department of Chemical Engineering, University of California, Santa Barbara.
[‡] Materials Research Laboratory, University of California, Santa Barbara.
[§] Department of Materials, University of California, Santa Barbara.
[||] Department of Physics, University of Fribourg.
[⊥] Nestle Research Center.

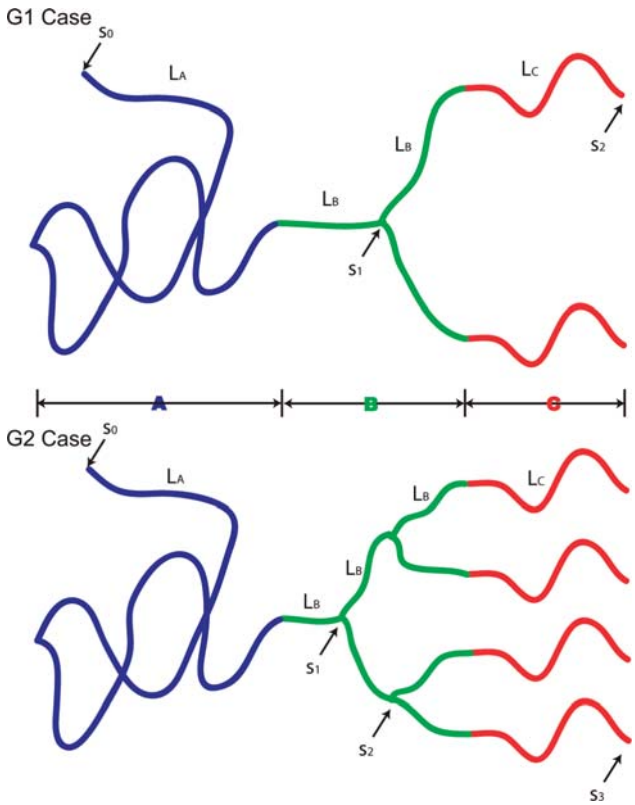

Figure 1. The molecular structure and block organization of both pitchfork-like dendritic copolymers investigated. The above and the below figures represent what are referred to as $G1$ and $G2$ structures, respectively, in the text. Branching junctions and end points are labeled s_i for both structures.

In the present paper, we apply this mean-field methodology to two dendritic "pitchfork-like" block copolymers, which are shown in Figure 1. This investigation was designed in order to compare these two molecular architectures and understand how their similar dendritic connecting blocks influence the regions of stable morphologies. In particular, this work explores cylindrical phase stability for these copolymers, with thin film applications in mind. The present study was inspired by three recent experimental studies.[22−25] In the following, we refer to the simpler of these copolymers, with the Y-junction middle block as a $G1$ dendrite, for its single "generation one" block splitting. The second is denoted as a $G2$ dendrite, with its two branches in the middle block.

2. The Coarse Grained Model and its SCFT Solution

The two dendritic copolymers of Figure 1 are modeled as branched copolymers composed of Gaussian threads that share many of the characteristics of the inhomogeneous polymers considered in previous studies.[26,29−31] As with many of these model systems, we assume the melt of these copolymers is incompressible and the interactions are described as contact-like Flory−Huggins repulsions between dissimilar blocks. While much of our analysis is now standard in the theory of inhomogeneous polymers,[26] we focus on the aspects that are pertinent to the connectivity and branching architecture unique to this system. For simplicity, we outline below the theoretical framework used to treat an incompressible melt of the more complicated $G2$ copolymers. The $G1$ copolymers were treated using a similar analytical framework that is a straightforward adaption of formalism below.

The canonical partition function for a melt of dendritic copolymers with three blocks, labeled A, B, and C, in the field representation can be written,[26]

$$Z \sim \int DW_A DW_B DW_C DP D\varphi_A D\varphi_B D\varphi_C e^{-H[W_i,\varphi_i,P]} \quad (1)$$

where H is an effective Hamiltonian in units of the thermal energy k_BT, and is a functional of the block densities φ_i, their conjugate fields W_i, and a pressure-like field P, which enforces incompressibility. The Hamiltonian is,

$$\alpha H/n = \frac{1}{V}\int d\mathbf{r}\left(\sum_{i<j} x_{ij} N\varphi_i\varphi_j - \sum_i W_i\varphi_i + P(\sum_i \varphi_i - 1)\right) - \alpha \ln Q[W_i] \quad (2)$$

where n is the number of copolymers in the melt and α is a scaling factor described below. The single chain partition function, $Q[W_i]$, contains the conformational entropy of the Gaussian chains experiencing the W_i potentials, including the effects of branching and block connectivity in the $G2$ architecture, and can be written,

$$\begin{aligned} Q[W_A, W_B, W_C] = & \int D\mathbf{r}\, e^{-U_0 - \int_{s_0}^{s_1} ds(\gamma_A(s)W_A + (1-\gamma_A(s))W_B)} / \int D\mathbf{r}\, e^{-U_0} \times \\ & \prod_{k=1}^{2} \int D\mathbf{r}_k\, e^{-U_0 - \int_{s_1}^{s_2} ds W_B} / \int D\mathbf{r}\, e^{-U_0} \times \\ & \prod_{l=1}^{4} \int D\mathbf{r}_l\, e^{-U_0 - \int_{s_2}^{s_3} ds(\gamma_B(s)W_B + (1-\gamma_B(s))W_C)} / \int D\mathbf{r}\, e^{-U_0} \quad (3) \end{aligned}$$

This expression is structured to reflect the architecture of the copolymer, which has two independent design features: the locations of the branching junctions in the $G2$ dendron, and the placement of the blocks within the structure. Each line of eq 3 corresponds to contributions to the partition function between branching junctions. The first portion is the pitchfork handle, which extends from the end point s_0 to the junction s_1, as labeled in Figure 1 (bottom), and identified in the top line of eq 3 above. The handle consists of blocks of A and B segments, which are distinguished by the function $\gamma_i(s)$, which is unity for the ith species block type, and otherwise zero. At point s_1 the copolymer branches into two equivalent B-block threads which extend to point s_2, and this is the contribution in the second line of eq 3 above. Finally, the four linear tines composed of B- and C-block segments contribute in the last line. Each section of copolymer includes the stretching energy of the threads, U_0, which, in units of k_BT, is

$$U_0 = \frac{1}{4R_{go}^2}\int_{s_i}^{s_{i+1}} ds \left|\frac{d\mathbf{r}_i(s))}{ds}\right| \quad (4)$$

for a polymeric segment beginning at s_i and ending at s_{i+1}. All blocks are regarded as equally flexible, composed of chemically distinct but otherwise equivalent segments.

We employ a reference radius of gyration, $R_{go} = b(N/6)^{1/2}$, which is that of an ideal *linear* triblock copolymer with the same end-to-end polymerization index as the polymers in Figure 1. The reference polymerization index, N, and that of the whole molecule, N_{TOT}, are expressed in terms of the individual block lengths L_i (see Figure 1),

$$N = L_A + 3L_B + L_C \quad (5)$$

$$N_{TOT} = L_A + 7L_B + 4L_C \quad (6)$$

The reference length scale R_{go} is a natural molecular scale for organization, and using it simply scales the Hamiltonian in eq 2 by the geometric ratio $\alpha = N/N_{TOT}$. Additionally, the relation in Eqn.6 determines the block volume fractions,

$$f_A = L_A/N_{TOT}, \quad f_B = 7L_B/N_{TOT}, \quad f_C = 4L_C/N_{TOT} \quad (7)$$

Note that these are total block volume fractions, as opposed to the equivalent triblock volume fractions, $\tilde{f}_i = L_i/N$.

In practice, the single chain partition function in eq 3 is evaluated by solving a modified diffusion equation for the (backward) chain propagator, and this method and the conditions for this procedure are described in more detail in Appendix 1. All calculations are performed within the context of self-consistent field theory (SCFT), a mean-field approximation, and some details of this approximation and the calculation are also included in Appendix 1. The intensive, mean-field free energy per chain in units of k_BT, $\alpha F/n = \langle \alpha H/n \rangle$ for various candidate phases is calculated and compared to determine the regions of stability. Architectural changes are monitored by varying the total block volume fractions, $f_i = \langle \varphi_i \rangle$, while keeping the $G1$ and $G2$ branch structures intact. Interactions are varied by means of the segmental Flory−Huggins block repulsions χ_{ij}.

3. Results

Two main results of this investigation are the mean-field phase diagrams for varing block compositions of the $G1$ and $G2$ architectures at a fixed set of interaction parameters. These are shown in Figure 2, parts a and b. Additionally, one mean-field phase diagram for a fixed composition of the $G2$ architecture with varying block incompatibilies is shown in Figure 6. The first two diagrams are discussed in the following subsection and an investigation of block incompatibility for the $G2$ structure follows in subsection 3.2. In both cases, we restrict our investigation to $1D$ and $2D$ structures, which are the best candidate phases in thin film applications.

3.1. Architectural Effects on Mesoscale Morphologies. The phase diagrams in parts a and b of Figure 2 vary the block compositions in the dendrons while maintaining block incompatibilities. The incompatibilities are fixed so that the A-block, largely the handle of the pitchfork, is incompatible with the C-block tines. The handle is, on the other hand, fully compatible with the B-blocks, which are the connecting blocks between the handle and tines. The B-block connecting portion is also equally incompatible with C-block tines, so that $\chi_{AC} = \chi_{BC} = 0.05$ and $\chi_{AB} = 0.0$. Essentially, the phase diagrams in parts a and b of Figure 2 are for copolymers with only two chemically distinct blocks, only the tines being distinct from the rest of the molecule.

We have chosen to explore architectural changes in these copolymers by adjusting the total block volume fractions of either the tines, f_C or the connecting B-blocks, f_B, which determine the handle fraction $f_A = 1 - f_B - f_C$. It is important to note that the block volume fractions $f_i = N_i/N_{TOT}$ are fractions of the *total* polymer mass, and not the block volume fractions of the analogous linear triblock $\tilde{f}_i = N_i/N$. This distinction is important because we maintain the end-to-end polymerization at $N = 1000$. A consequence of this construction is that the total polymerization, N_{TOT}, is *not* fixed with changes in f_i.

Though monitoring the total block fractions is natural, working at constant N is perhaps not as intuitive. There are, however, benefits of this construction. As mentioned before, the microdomain period is controlled by the radius of gyration of an ideal triblock of equivalent length, $R_{go} = b(N/6)^{1/2}$, and the energy of incompatibility is $\chi_{ij}N$, both natural scales for mesophase organization of these dendritic copolymers.

A limiting architecture of both pitchfork copolymers of Figure 1 is $f_B \rightarrow 0$, which shrinks the connecting, B-block segments to a simple connecting junction. In this limit, the handle of the pitchfork is tethered directly to the incompatible C-block tines, creating an A−C_4 mikto-polymer. Although $f_B = 0$ is outside the plotted regions of Figure 2, it is a reasonable starting benchmark for understanding the phase diagrams. Increasing f_B from zero, at fixed tine fraction f_C, corresponds to moving more mass from the handle of the pitchfork to the connecting, dendritic B-block segments. Since the B-blocks are chemically

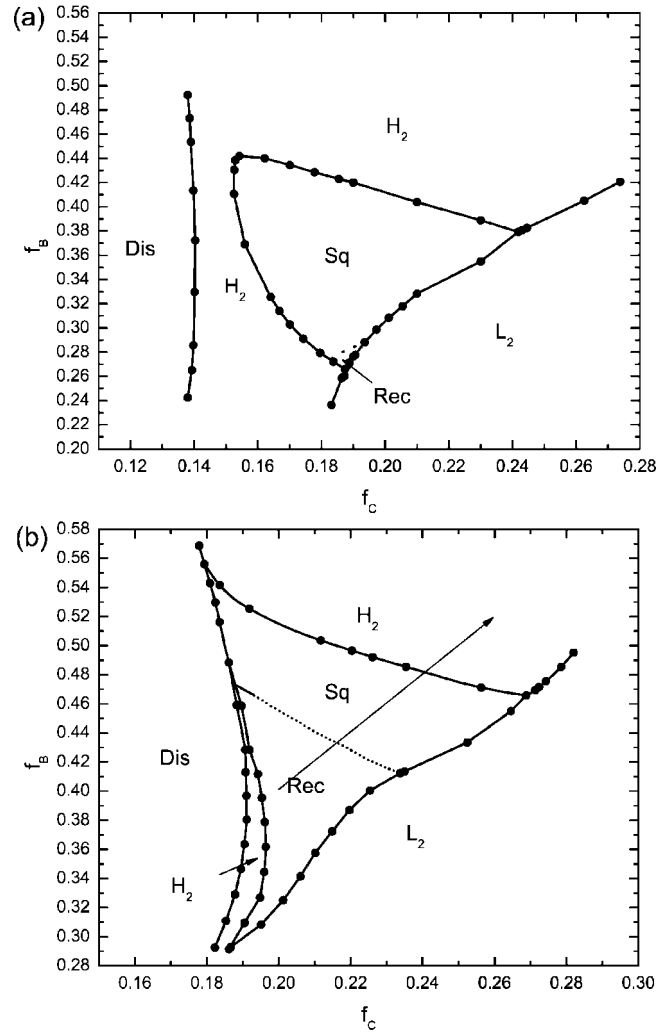

Figure 2. Mean-field phase diagrams for the $G1$ and $G2$ dendritic copolymers in composition coordinates f_B and f_C. The incompatibilities are set with $\chi_{AB} = 0$, $\chi_{AC} = 0.05$, $\chi_{BC} = 0.05$, and the end-to-end polymerization is maintained at $N = 1000$. Note that in these diagrams the A- and B-blocks are chemically indistinguishable. The phase diagram of the $G1$ dendron, a copolymer with a middle block that forks once to attach to two C-block tines, is shown in the top figure (a). The phase diagram of the $G2$ structure, which has a middle block that forks twice to connect to four tines, is shown below in part b. The labeled phases are *Dis*, the homogeneous phase; H_2, a large hexagonal phase; *Sq*, the square phase; *Rec*, the rectangular phase; and L_2 large lamellar phase. See the text for a discussion of these diagrams, including the arrow drawn in part b.

indistinguishable from the A-blocks, this is a simple shifting of the mass, albeit with implications for polymer conformational entropy. As mentioned above, in this process, the end-to-end length N is maintained, so that the pitchfork length is fixed. However, increasing the connecting fraction f_B causes the total degree of polymerization, the sum over all blocks, N_{TOT}, to *grow*. Note that the process of shifting mass from the pitchfork handle to the connecting B-blocks traces vertical trajectories in parts a and b of Figure 2.

Two common regimes of the phase diagrams in Figure 2 are simply explained. First, since the C-blocks are the only incompatible blocks, when f_C is very small, too little of it is present to assemble into organized structures in the melt and only a disordered phase is present. This is evident for tine compositions of roughly $f_C \leq 0.14$ for the $G1$ copolymer and $f_C \leq 0.18$ for the $G2$ structure. At these low f_C values, changing the pitchfork architecture with f_B has essentially no effect; moving some of the molecular mass from the handle to the

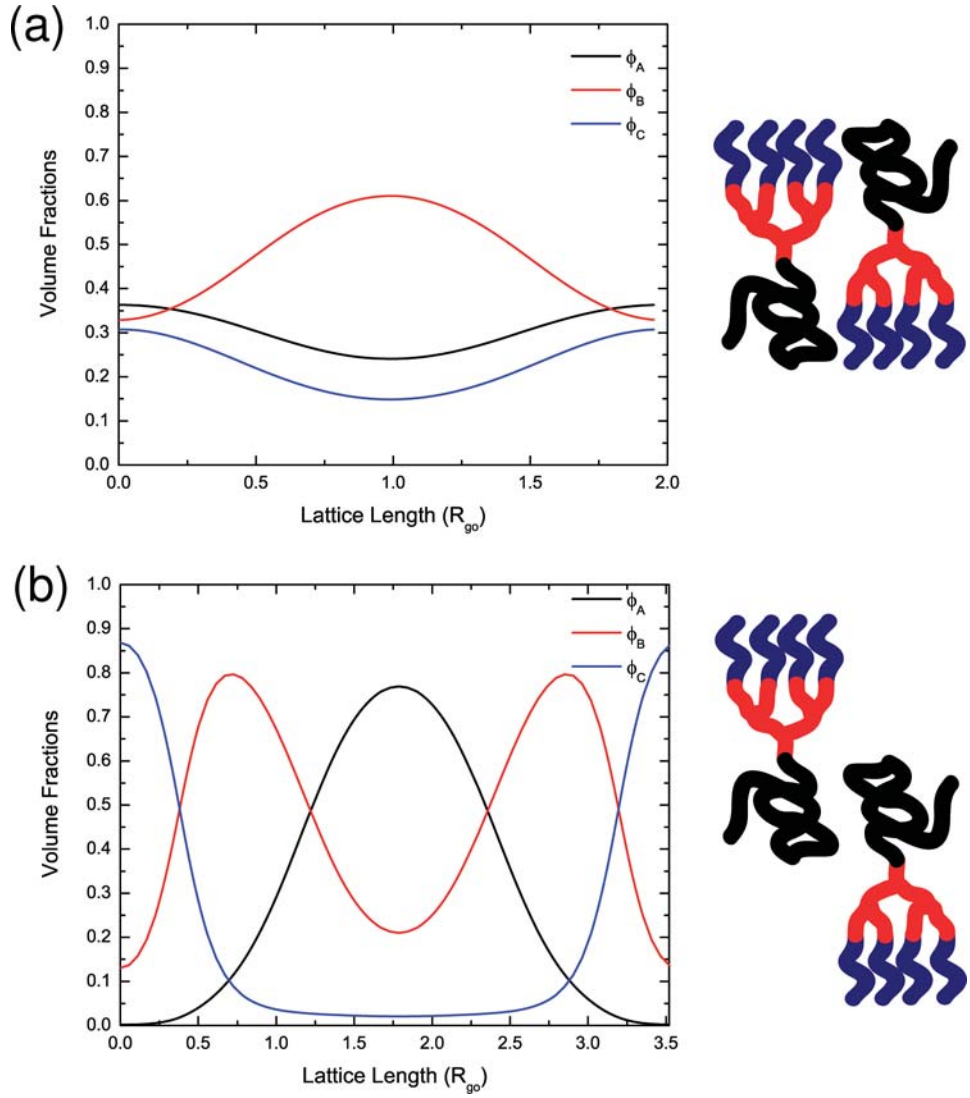

Figure 3. Density profiles for the two types of lamellar phases. The lamellar phase L_1 has a smaller lattice size and is shown in part a. The larger stacking L_2 lamella is shown in part b. The L_1 stacking is A/C−B−A/C−B... (the *B* dendritic linker is isolated by a sheet of mixed A and C densities). In this case, the tines and the handles of the forks are coincident. The larger L_2 stacking is C−BAB−C−BAB−*C*... and the forks are stacked, back-to-back, with interlocking tines. The tines and handles form distinct layers. The left-sided schematic diagrams show the molecular stackings of L_1 and L_2 lamella phases.

connecting (B) segments does not change the melt's ability to organize into structures. Second, at small f_B and large f_C values, the copolymer is composed of long A-block handles tethered to two or four, incompatible C-blocks. These copolymers favor stacked lamellae, L_2, where isolated sheets of C-blocks form, surrounded by layers of the other blocks. This phase has stretched, interdigitating C-block tines, like two forks stacked end-to-end with entangled tines. The density profile for this lamellar phase is shown in Figure 3b, and the C-block lamellae are separated by stacks of *B* and *A* layers. The layer stacking is C−BAB−C−BAB−.

While these limiting regions are fairly easy to understand, the crossover between them is more complicated. Between these limiting cases, we focus on a range of compositions in parts a and b of Figure 2 in which the C-block is the minority component by volume, so that the incompatible tines of the copolymers are segregated into discrete domains surrounded by a medium of the other blocks. The opposite case, a composition range that describes a melt of dendritic copolymers with short incompatible handles, which create cylinders of A-blocks surrounded by a continuous medium mostly of C tines[32] is not considered in these figures. The plotted composition ranges in Figure 2 are focused on the formation of cylindrical phases that *oppose* the natural, widening curvature of the copolymers; it is the type C tines that are confined into domains.

In Figure 2a, increasing f_C from small concentrations beyond the threshold for structural assembly, the C-block tines segregate into cylinders that pack into a hexagonal lattice. A further increase in the tine length may bring about the square (*Sq*) or the rectangular (*Rec*) lattice, but eventually the longer tines stretch to fill a sheet and lamellar (L_2) stacking results. A similar sequence is found for the *G*2 architecture in Figure 2b.

Since this is a two-block copolymer (the A- and B-blocks are chemically indistinguishable), we interpret this phase sequence to be somewhat analogous to that of a simple diblock copolymer. At modest incompatibilities in the melt, increasing the size of the short, incompatible block of a diblock brings about a transition from the homogeneous phase (*Dis*) to ordered mesophases, 3*D* and 2*D* structures respectively, and then stacked lamellae.[8−10] Similarly, in these dendritic systems, increasing the portion of tethered incompatible blocks, f_C, at a fixed f_B, causes a similar set of transitions, *Dis* to 2*D* structures to L_2. The dendritic *B* -block connector only changes the size and shape of the stability region and the nature of the favored 2*D*

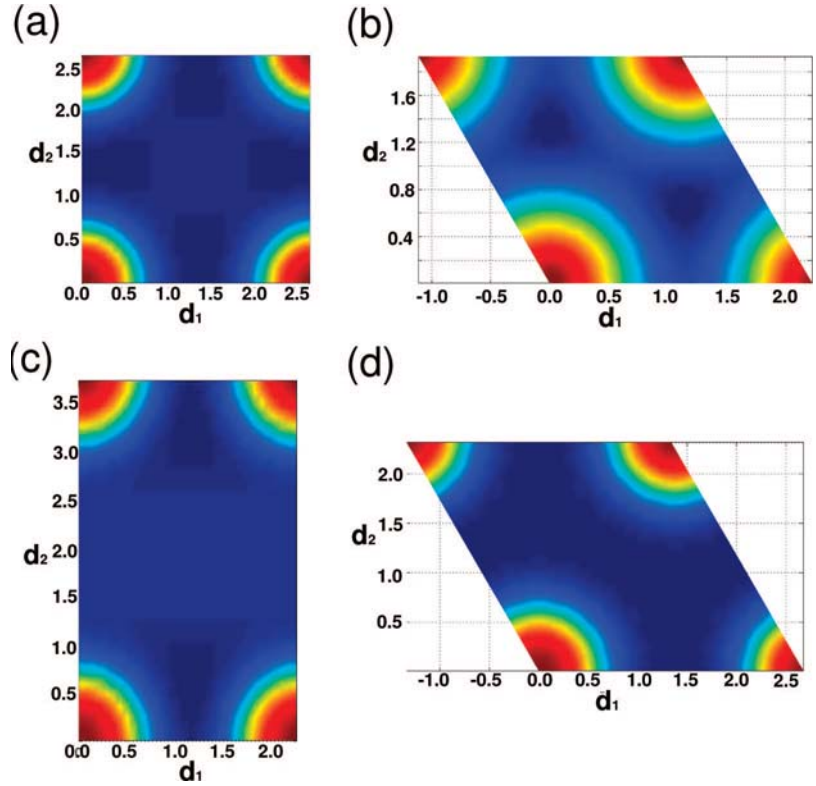

Figure 4. Density profiles for four types of two-dimensional cylindrical phases: (a) the square phase (*Sq*), (b) the close-packed hexagonal phase (H_1), (c) the rectangular phase (*Rec*), and the larger lattice hexagonal phase (H_2). The circular (cylindrical) domains are regions of high C-block (tine) density. Note the difference in lattice spacing for the hexagonal phases.

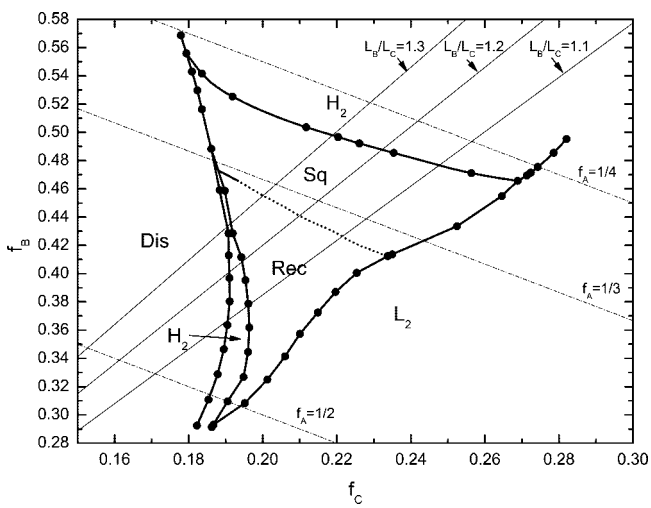

Figure 5. Mean-field phase diagram (Figure 2b) for the *G*2 copolymer with some architectural guide lines for the handle volume fractions: $f_A = {}^1/_2,\ {}^1/_3,\ {}^1/_4$. The segment polymerization ratios $L_B/L_C = 1.1,\ 1.2,\ 1.3$ are also indicated.

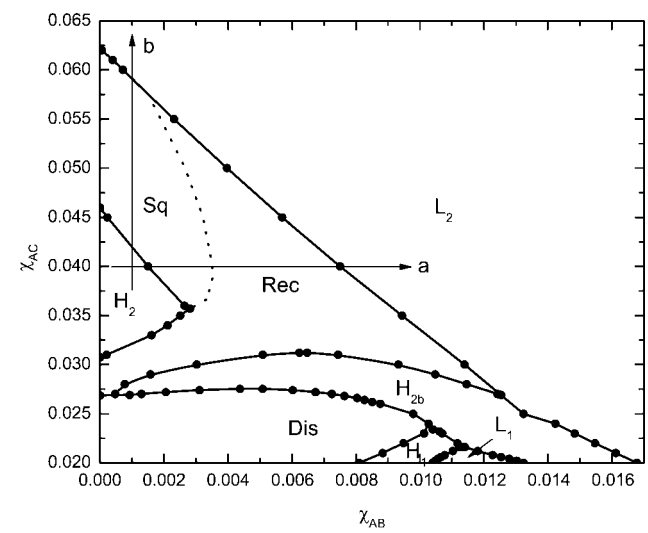

Figure 6. Mean field phase diagram of a fixed *G*2 architecture in coordinates of the interaction parameters, χ_{AC} and χ_{AB} with $\chi_{BC} = 0.05$. The copolymer has the compositions $f_A \simeq 0.303$, $f_B \simeq 0.472$, $f_C \simeq 0.225$, and $N = 1000$. The labeled phases are *Dis*, the homogeneous phase; H_1, the small-lattice hexagonal phase; H_2, the larger hexagonal phase; H_{2b}, a *swollen* H_2 phase; *Sq*, the square phase; *Rec*, the rectangular phase; L_1 the small-lattice lamellar phase; and L_2, the large-lattice lamellar phase. The a and b arrows represent the two trajectories considered in Figures 9 and 10 respectively.

phases. We may expect more complicated 3*D* phases to lie near the *Dis* cusp in Figure 2, parts a and b. For brevity we have neglected the stability regions of these 3*D* phases (if any), and Figure 2, parts a and b, shows the simpler set of transitions, *Dis* to 2*D* -phases to L_2. Some of these phase sequences are consistent with experimental results.[22−25,33]

Increasing the composition of the connecting *B* -blocks, f_B, causes the width of the 2*D* phase stability regions to grow in Figure 2, parts a and b. Clearly, shifting some of the polymeric mass to the dendritic middle block is essential to stabilizing the 2*D* phases, including the square-packed (*Sq*) and rectangular (*Rec*) phases. This may be more simply understood by considering the opposite trend: the reduction of the connecting blocks, $f_B \rightarrow 0$, which tether the multiple C-block tines directly to an incompatible handle. The C-block core domains filled with tines become increasingly difficult to assemble with decreasing f_B, as this reduction opposes the natural curvature of the copolymers. This diminishes the basin of 2*D* phase stability for both the *G*1 and *G*2 architectures, though the region markedly retracts

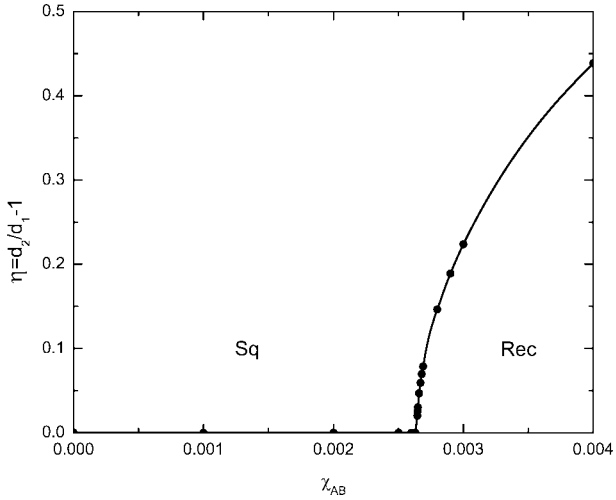

Figure 7. Structural order parameter $\eta = d_2/d_1 - 1$, for the square to rectangular transition of the *G*2 copolymer as a function of the interaction parameter χ_{AB}. The lattice spacings for the cubic phases are d_1 and d_2, and the transition signature for the order parameter $\eta = d_2/d_1 - 1$ is continuous, with the d_2 spacing growing continuously from d_1 from the transition. The incompatibilities are $\chi_{AC} = 0.05$ and $\chi_{BC} = 0.05$.

for the *G*2 architecture, whose four tines more strongly oppose the reversed domain curvature.

Starting from the lower left portion of the phase diagram for the *G*2 architecture, and progressing to the upper right with a fixed volume fraction ratio, $f_B/f_C \approx 2$, the phase sequence, starting from *Rec* is *Rec* → *Sq* → H_2 (see the arrow drawn on Figure 2b). This phase progression takes place with a linear depletion of the total *A* fraction in the system, i.e. a shortening of the fork handle (see Figure 5). By diminishing the *A* -block handle, the interstitial space between the organized C-block cylindrical domains retracts. The domains arrange correspondingly, from a rectangular phase, where the surrounding media is expansive to accommodate the long *A* -block handles, to square packing for somewhat shorter handles, to hexagonal packing for short handles. Density profiles for these phases can be seen in Figure 4. The condition for the stable *Sq* phase is similar to that of the ABC triblock copolymer melt case[34] since the A handle occupies the interstitial area. However, the bulky dendron structures space the A handles away from the C cores in our case rather than the linear B block between A and C blocks in the ABC triblock case. In addition, the phase sequence predicted by our model (*Dis* → *Rec* → *Sq* → L_2) with fixed f_B is consistent with available experimental results.[22−25]

All transitions in the phase diagram in Figure 2b are first order with the exception of one, which is drawn with a dashed line. This is the *Sq* to *Rec* transition, which is a *continuous* transition, and will be discussed in more detail below. One boundary of this transition is difficult to resolve and an extrapolation is drawn with a solid line. The determination of this boundary requires a prohibitive resolution in order to resolve the free energies, likely due to the weak signature of the transition.

3.2. Phase Stability of the *G*2 Dendritic Copolymer with Changing Block Incompatibilities. As described above, stable hexagonal, square and rectangular mesophases can be found for regions in block composition with a fixed set of incompatibilities. Here we present another phase diagram, Figure 6, that explores the stable phase morphologies of a single, fixed-composition *G*2 copolymer with changing block interactions. The *G*2 copolymer considered has the structural parameters $f_A \simeq 0.303$, $f_B \simeq 0.472$, and $f_C \simeq 0.225$, which create a stable square phase for the interactions employed in Figure 2b.

For this architecture, rather than changing the composition, two incompatibilities are varied, χ_{AB} and χ_{AC}, while maintaining constant $\chi_{BC} = 0.05$. Since square packing is desirable symmetry, we focus on its basin of stability and the limiting transitions to other structures. Two interactions with the handle A blocks can destabilize the phase, and the following subsection considers the effects of the handle interactions with the connecting B-block segments. Subsequently, subsection 3.2.2 investigates the destabilization of the phase due to interactions of A handles with the C-block tines. Subsection 3.2.3 explores other types of structural assembly in this system well outside the region of stable square packing.

3.2.1. Stability of the Square Phase with Changes in the A−B Block Incompatibility, χ_{AB}. Starting from the incompatibilities $\chi_{AC} = 0.05$ and $\chi_{AB} = 0.0$, i.e., those of Figure 2b, we find a fairly limited window for the stability of the *Sq* phase in Figure 6. Either changing χ_{AC} or increasing χ_{AB} destabilizes this symmetry. The increase of χ_{AB} causes the handle and connecting B-blocks to stretch, minimizing their regions of contact with the C-rich circular domains. By stretching this portion of the pitchfork, the interstitial space between the domains must grow to accommodate the longer dendritic, connecting blocks (and handles) and the *Sq*→*Rec* transition takes place. In Figure 5 tracing the arrow backward corresponds to physically lengthening the handle of the fork, i.e., increasing f_A. This increase in the handle length destabilizes the *Sq* phase and brings about the *Sq* → *Rec* phase in Figure 5, a phenomenon similar to the stretching effects caused by the incompatibility χ_{AB} in Figure 6.

Further investigation of the *Sq* → *Rec* transition indicates that it is an unusual one with a continuous change of symmetry. To explore this feature, it is convenient to define an order parameter that allows us to quantify and monitor the structural changes in the transition. The rectangular phase is described structurally by two lattice parameters, d_1 and d_2, which correspond respectively to the short and long lattice spacings of the symmetry. When the rectangular phase retracts to a square lattice, the long lattice spacing, d_2, contracts to d_1 and the ratio d_2/d_1 is unity. A convenient structural order parameter for the *Sq* → *Rec* transition is thus, $\eta = d_2/d_1 - 1$, which vanishes for square packing and is greater than zero for the rectangular phase. The evolution of the order parameter across the *Sq* to *Rec* phase boundary for $\chi_{AC} = 0.05$ and changing χ_{AB} is shown in Figure 7. This transition is indeed continuous.

In the *Rec* phase, if the incompatibility χ_{AB} is increased further, the handle and connecting B-blocks stretch further, and the rectangular lattice swells. The density plots of Figure 8 show the lattice swelling in the rectangular phase. This dilation brings about a minimal change in the C-block cores but causes the A- and B-block density profiles to significantly change with the increase in χ_{AB}. At lower χ_{AB}, in the rectangular phase (panel a in Figure 8), the A-block handles inhabit cylindrical domain cores spaced in a regular rectangular array staggered from the C-block domain lattice. Increasing χ_{AB} causes the A-block domains to delocalize, and they form a thick, undulating lamellae that expels the B-blocks out of the layer and dilates the rectangular lattice spacing, as shown in Figure 8, panels b and c. The B-blocks remain expelled from the C-cores due to the high χ_{BC} incompatibility and the C-rich domains periodically decorate the wavy lamellae. A stable rectangular phase results, comprised of stretched handles and stretched connecting *B*-block segments, their aversion mediated by χ_{AB}.

This stretching and swelling continues with a further increase in χ_{AB} until the B-blocks lengthen to a threshold where a flat interface with the C-block domains becomes favorable. The circular C-block cores become too energetically costly, and the melt undergoes a transition to the L_2 lamellar phase. The lamellar

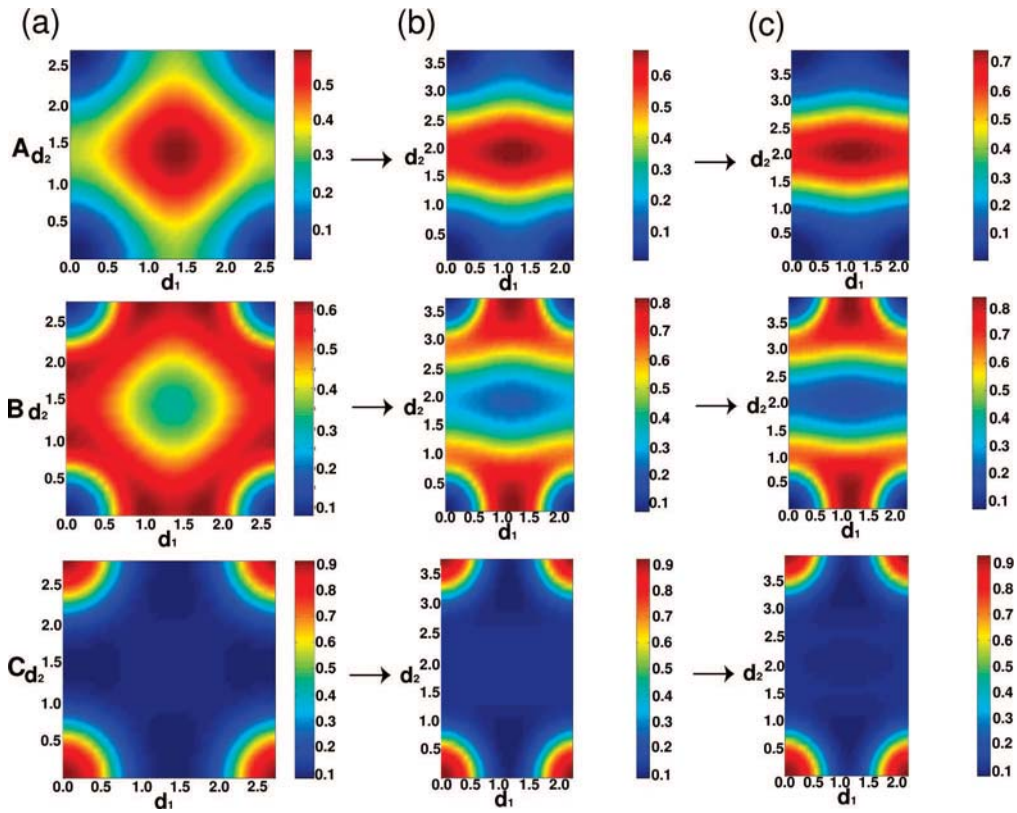

Figure 8. Contour plots of the block densities in the rectangular phase at various swellings mediated by χ_{AB}. The top, middle, and lower rows show the A-, B-, and C-block densities, respectively. The A-block domains in the middle of the unit cell of panel a, top, delocalize to form undulating lamellae, which are shown in the top row of panels b and c. The lamellae are periodically decorated with C-block domains on the unit cell verticies (see the lowest row) which are essentially unchanged in the swelling. Note the scale changes in each unit cell, which indicate a dilation of the cell along the long axis with the increasing χ_{AB}. The incompatibilities are $\chi_{AC} = 0.04$, $\chi_{BC} = 0.05$ for all panels and $\chi_{AB} = 0.0035$ in panel a, $\chi_{AB} = 0.0059$ in panel b, and $\chi_{AB} = 0.0075$ in panel c. A swelling of 5.3% is observed for d_2 when going from b to c.

stacking is the same as before: the C-block interlocking tines of the end-to-end forks are well separated by stacks of BAB layers. The lattice spacing is large due to the chain stretching which necessarily separates the A-, B-, and C-rich portions of the lamellar stacking.

Figure 9 shows the volume averages of all binary interactions in the system and the chain entropy for a trajectory along χ_{AB} with $\chi_{AC} = 0.04$ fixed, which includes the $Sq \rightarrow Rec \rightarrow L_2$ sequence. Starting within the rectangular phase, the A/C interaction decreases as these densities are isolated with the swelling depicted in Figure 8. The B/C interaction energy slightly grows, but the A/B energy increase associated with the swelling of the rectangles is sizable, reflecting the pivotal role of the reorganization of the B-density around the undulating lamellae in the dilation of this phase. The $Rec \rightarrow L_2$ transition, which is clearly first order, shows that the reorganization of the densities involved creates a more favorable energetic configuration since *all* energies decrease with this transition, but is accompanied by a large entropic penalty due to the stretched chains that comprise it. As a final note regarding Figure 9, the $Sq \rightarrow Rec$ transition can be further identified as a continuous one by the slope discontinuities and concomitant equal energies and entropies at the phase boundary.

3.2.2. Destabilization of the Square Phase with the Handle−Tine Interaction, χ_{AC}. Figure 10 shows the volume averaged binary interaction energies for a separate trajectory in the phase diagram of Figure 6. This examines the stability of the square phase with changes in χ_{AC}, while χ_{AB} is fixed: a vertical trajectory on this phase diagram. Note that within the individual phases, nearly all energies decrease with a growing χ_{AC} but this competes with a growing entropic penalty. The $H_2 \rightarrow Sq$ transition has very small entropic and energetic changes upon structural reorganization.

Also, the $Sq \rightarrow L_2$ transition, which is not separated by a *Rec* phase along this trajectory, shows that the A and C density reorganizations are the most important in this transition. The A/C interaction energy drops most precipitously in the $Sq \rightarrow L_2$ transition due to the isolation of the A and C layers in the L_2 lamellar stacking, which consists of C layers separated by BAB stacks. The A and C layers have very little coincident density in this geometry. The density reorganization in the $Sq \rightarrow L_2$ transition is energetically favorable for all block species with the exception of B and C overlap. Creating a planar interface, which increases the total amount of B/C interface in the system, causes the positive jump in the B/C interaction energy across this transition.

3.2.3. Other Regions of the Phase Diagram, Figure 6. Beyond the window of *Sq* stability, there is an impressive number of packing morphologies available to this system with changing block incompatibilities. There are *seven* different mesophase morphologies for this one-component melt in Figure 6, without considering 3*D* structures. The *Dis* phase at low compatibilities χ_{AB} and χ_{AC}, is prominent because the A-block handle is long and the only incompatible portions of the copolymer are the comparably small connecting B-block segments and C-block tines. Even at the modest B/C interaction strength $\chi_{BC} = 0.05$, these portions of the pitchfork are not sizable enough to overcome the translational and conformational entropy and bring about mesophase organization.

However, increasing either of the incompatibilities *with the handle*, χ_{AB} or χ_{AC}, can generate mesophases. We consider the phase symmetries first at small χ_{AC} and moderate χ_{AB}. In this

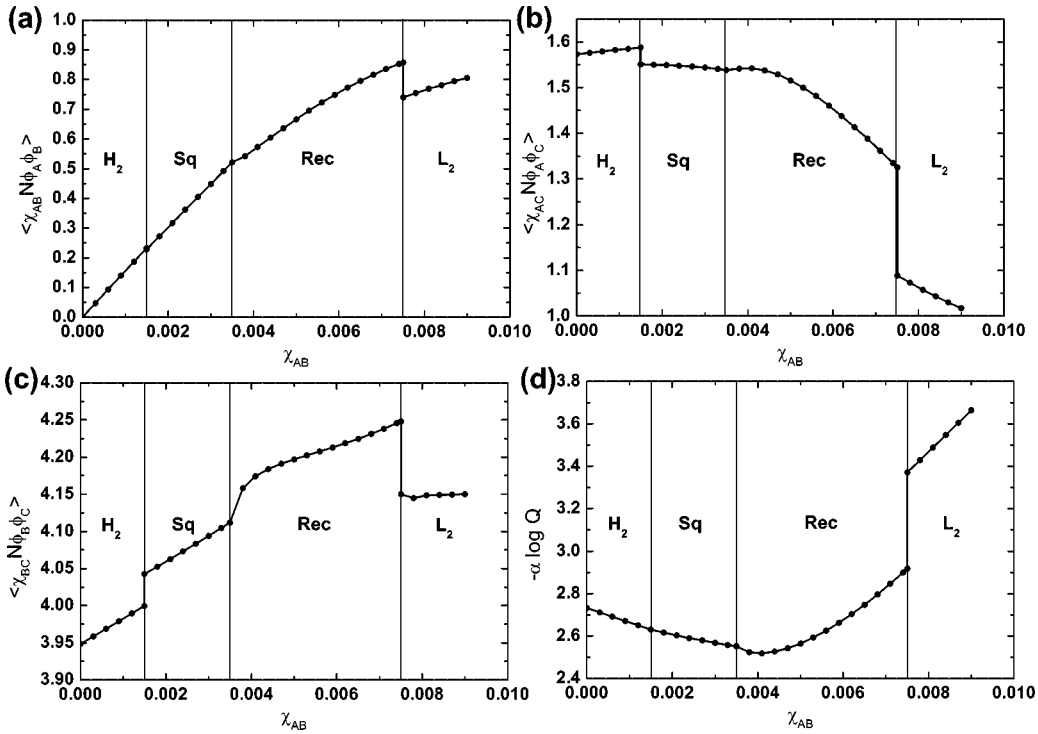

Figure 9. Volume averaged binary interaction energies and entropy as a function of χ_{AB} with $\chi_{AC} = 0.04$ and $\chi_{BC} = 0.05$ fixed. The panels show the A/B interaction energy (a), the A/C interaction energy (b), the B/C interaction energy (c), and the contribution of the chain entropy to the free energy, $-\alpha \log Q$ (d). Note the scale changes on the vertical axes.

region of the phase diagram there is a different lamellar phase, L_1. Its density is plotted in Figure 3a and consists of a different stacking from L_2. The A-rich layer overlaps with the C-block tines, since their repulsion is small, and the B-density is weakly segregated from the A/C surrounding layers. This stacking has *two* alternating layers, B−A/C−B−A/C−B−..., rather than the three distinct layers of the BAB−C−BAB−C... stacking of L_2. In the L_1 lamellar stacking, the forks are stacked end-to-end, but the tines are coincident with the handles of neighboring forks. Because of this arrangement, L_1 has a much shorter lattice spacing. This phase is sensitive to changes in χ_{AC} due to the significant overlap in the A- and C-block densities. Upon increasing χ_{AC}, L_1 is destabilized into a swollen hexagonal phase, H_{2b}, and then into L_2.

In the same region of this phase diagram, bordering the L_1 lamellae, is the hexagonal cylinder phase H_1. This phase is the analogous phase to L_1 but with hexagonal symmetry. As in L_1, the A and C blocks have coincident densities in H_1, forming a mixed A/C core surrounded by an interstitial medium comprised of the connecting *B* -blocks. Rather than the cores containing only the C-block tines of end-to-end stacked forks in H_2, the H_1 circular domains contain the C-block tines mixed with A-block handles. Because of this packing, the lattice spacing for H_1 is also comparably small compared to H_2.

As might be expected with heavily overlapping A and C densities, the H_1 phase is also sensitive to χ_{AC}. Increasing χ_{AC} destabilizes it, and a transition to *Dis* (at lower χ_{AB}) or H_{2b} (at higher χ_{AB}) takes place. The phase H_{2b} is a similar hexagonally packed structure to H_2, but has a larger unit cell because the interstitial medium is comprised of stretched A- and B-blocks. This is, to our knowledge, the only *Hex* → *Hex* transition in copolymers in any investigation, and is rather unique because it takes place in such a simple system, a single component melt. However, it is possible, and perhaps likely, that with a consideration of 3*D* structures this transition might be preempted by one or more other structural transformations. At larger χ_{AC} or χ_{AB} values, the L_2 phase is again present. The large repulsive energies are minimized in this geometry, overcoming the entropic penalty of the stretched chains.

4. Summary and Discussion

Mean-field theory has been applied to two melts of dendritic triblock copolymers with pitchfork-like shapes to investigate their ability to assemble into unique equilibrium mesophase structures. These dendritic architectures have been chosen with thin film studies in mind. In particular, similarly shaped copolymers in recent experiments[17,18,21−25] have exhibited square or rectangular phases, which are desirable for patterning thin films in microelectronic applications.

To mimick the copolymer structure of the dendronized combs in two recent studies,[22−25] this investigation has considered dendritic copolymers with three blocks in a rather limited composition range. These are pitchfork-shaped dendritic copolymers with relatively short incompatible tines. In the composition range we consider, the tines are generally incompatible with the rest of the melt and form discrete domains separated from the interstitial medium of handles and connecting segments. This is an unusual arrangement because it is the *tines* that are forced into the minority domains with curved interfaces. This assembly opposes the natural curvature of the molecule and form because of the relatively small chain length of the tines, and their incompatibility with the other blocks. Our findings are in remarkably good qualitative agreement with a recent real space study of similar dendron polymer systems.[24,25] The opposite limit, which is a melt of copolymers with short incompatible *handles* and longer connecting blocks and tines, form discrete domains of segregated handles.[32] This domain assembly is commensurate with the curvature of the copolymers, but is not considered in this investigation.

Both copolymer architectures, denoted *G*1 and *G*2 for the single and double forking in their middle B blocks, have stable regions of square (*Sq*) and rectangular (*Rec*) phases. The *G*1 copolymer has a region of *Sq* packing and a very limited region

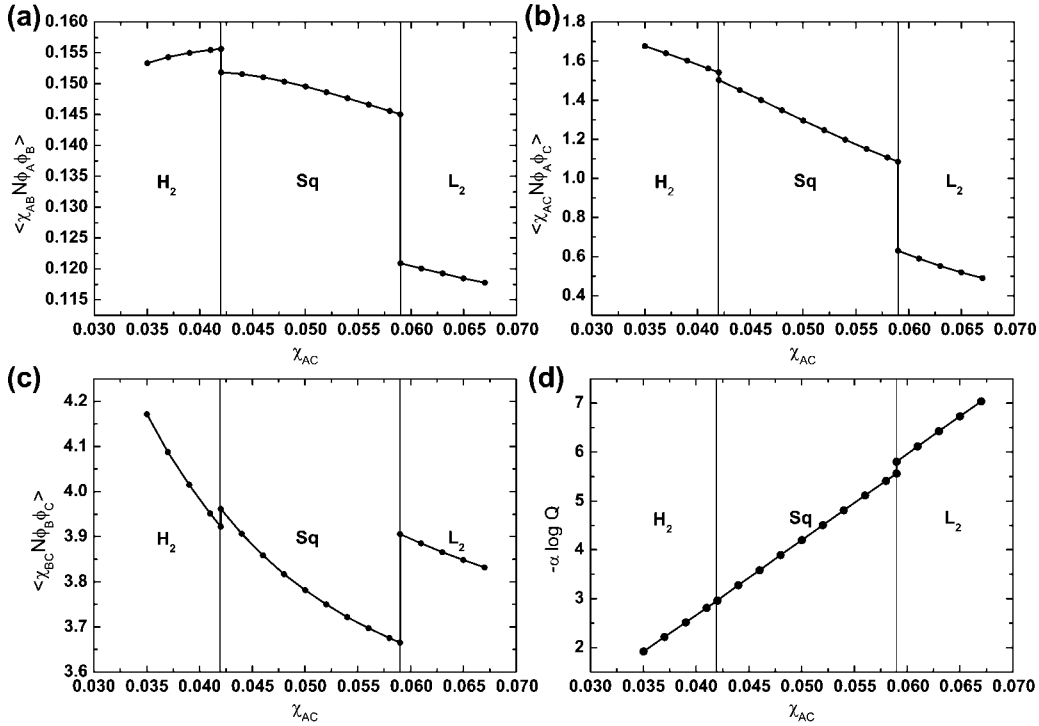

Figure 10. Volume averaged of binary interaction energies and entropy energy as a function of χ_{AC} with $\chi_{AB} = 0.001$ and $\chi_{BC} = 0.05$ fixed. The plots are ordered as in Figure 9, with *A*/*B* interaction energy (a), the A/C interaction energy (b), the B/C interaction energy (c), and the negative chain entropy, $-\alpha \log Q$ (d). Note the changes in scale in the ordinate.

of stable *Rec* phase shown in Figure 2a. This is a phase diagram for a two-block copolymer: one with a fully compatible middle dendritic block and incompatible tines. As the middle *Y*-shaped block is diminished, the *Sq* and *Rec* phase regions contract and disappear. This is also the case for the *G*2 copolymer, shown in Figure 2b, which has a much larger region of *Rec* phase stability. The contraction of the *Sq* and *Rec* phases is more pronounced for the *G*2 structure because of its greater opposition to packing into domains with reversed curvature. In this case, as the connecting B-blocks contract, the four tines connect more directly to the handle, which is an arrangement for interfaces separating four tines packed into a cylindrical domains and surrounded largely by a medium of handles.

From these two phase diagrams in Figure 2, it is clear that not only is the dendritic structure of the connecting segments essential for stabilizing the *Sq* and *Rec* phases, this connecting block segment must also comprise a certain fraction of the copolymer. Furthermore, this middle dendron must be relatively compatible with the handle, as demonstrated in Figure 6. As the repulsion of the middle block with the handle is slightly increased, the *Sq* phase undergoes a continuous transition to a swollen *Rec* phase, and then lamellar stacks form. The handle/middle-block (A/B) incompatibility disrupts the square phase morphology at fully an order of magnitude *less* than than the handle-tine (A/C) incompatibility.

In addition to these square and rectangular phases, several other phases were uncovered for this system, including hexagonal phases for certain ranges of incompatibility. A *G*2 copolymer with incompatible tines that packed into the *Sq* phase in Figure 2b transforms into several other mesophases upon changing the block incompatibilities. Notably, for small tine-handle (A/C block) incompatibilities, other distinct lamellar (L_1) and hexagonal (H_1) structures were found. These morphologies have commensurate(mixed) handle and tine densities in closely packed discrete domains separated by a B-block density matrix. A first order transition separating *two* distinct hexagonal phases was also found, an unusual phenomenon in such a simple, one-component melt.

In performing these calculations, several of the usual assumptions and approximations have been employed that have a remarkably successful track record in the field-theoretic description of polymeric melts. The Flory−Huggins form of contact-like repulsions between dissimilar Gaussian blocks combined with the constraint of incompressibility comprise the usual set of approximate theoretical ingredients for the optimization of the block densities in a unit cell. Additionally, although recent work has made significant progress in including fluctuation-induced effects[35,36] in block copolymers, their effects are computationally demanding and are generally limited to order−disorder boundaries so that they have not been considered in this investigation. We have also neglected three-dimensional structures to lower the computational expense of the study. While these more complicated structures may alter the phase diagrams computed above, it is our expectation that they occupy regions near the order−disorder and *Lam*−*Hex* lines in the melt, and usually do not preempt the stability of the two-dimensional morphologies. Moreover, in thin film applications, complex cubic phases are often suppressed by wetting constraints on the substrate and top surface of the film.

Acknowledgment. This work was supported by the MRSEC Program of the National Science Foundation under Award No. DMR05-20415.

Appendix

In Appendices I and II, we present our theoretical formalism for the *G*2 architecture as outlined in the text. The framework for the *G*1 copolymer is straightforward simplification of that given below, with only one branch point.

I. Solving the Model in the Self-Consistent Field Theory Approximation. The single chain partition function in Eq. 3 is calculated using a *backward* propagator, $q^{\dagger}(r, s)$, which satisfies the modified diffusion equations with the initial condition $q^{\dagger}(r, s_3 = 0) = 1$. The diffusion equation it satisfies is,

$$\frac{\partial q^{\dagger}}{\partial s} = R_{go}{}^2 \nabla^2 q^{\dagger} - W_i q^{\dagger}, \tag{8}$$

with,

$$W_i = \begin{cases} \gamma_B W_B + (1-\gamma_B) W_C, & \text{if} \quad s_3 = 0 < s < s_2 \\ W_B, & \text{if} \quad s_2 < s < s_1 \\ \gamma_A W_A + (1-\gamma_A) W_B, & \text{if} \quad s_1 < s < s_0 = 1. \end{cases} \tag{9}$$

Additionally, the conditions for branching are,

$$q^{\dagger}(\mathbf{r}, s_2^L) = (q^{\dagger}(\mathbf{r}, s_2^R))^2 \text{ and } q^{\dagger}(\mathbf{r}, s_1^L) = (q^{\dagger}(\mathbf{r}, s_1^R))^2. \tag{10}$$

where L and R represent the limits found by approaching from either the left or right, i.e.

$$s_i^L = s_i + \varepsilon, \ \varepsilon \to 0^+ \text{ and } s_i^R = s_i - \varepsilon, \ \varepsilon \to 0^+ \tag{11}$$

Upon solving the diffusion equation for the propagator, the single chain partition function is simply evaluated,

$$Q[W_i] = \frac{1}{V} \int \mathrm{d}\mathbf{r} \, q^{\dagger}(\mathbf{r}, 1) \tag{12}$$

All calculations are performed within the context of self-consistent field theory (SCFT), a mean-field approximation, although, in principle, full fluctuating "field-theoretic simulations" can be performed.[26,37] The SCFT approximation assumes that the partition function is dominated by a single field configuration $\{\varphi_A^*, \varphi_B^*, \varphi_C^*, W_A^*, W_B^*, W_C^*, P^*\}$ and fluctuations about this configuration are wholly discarded. This condition is obtained when the effective Hamiltonian in eq 2 is extremized with respect to the fields, $\{\varphi_i, W_i, P\}$. This optimization results in the seven conditions

$$\varphi_A(\mathbf{r}) = -\frac{1}{Q}\frac{\delta Q}{\delta W_A}, \tag{13}$$

$$\varphi_B(\mathbf{r}) = -\frac{1}{Q}\frac{\delta Q}{\delta W_B}, \tag{14}$$

$$\varphi_C(\mathbf{r}) = -\frac{1}{Q}\frac{\delta Q}{\delta W_C}, \tag{15}$$

$$W_A(\mathbf{r}) = \chi_{AB} N \varphi_B(\mathbf{r}) + \chi_{AC} N \varphi_C(\mathbf{r}) + P, \tag{16}$$

$$W_B(\mathbf{r}) = \chi_{AB} N \varphi_A(\mathbf{r}) + \chi_{BC} N \varphi_C(\mathbf{r}) + P, \tag{17}$$

$$W_C(\mathbf{r}) = \chi_{AC} N \varphi_A(\mathbf{r}) + \chi_{BC} N \varphi_B(\mathbf{r}) + P, \tag{18}$$

$$\varphi_A(\mathbf{r}) + \varphi_B(\mathbf{r}) + \varphi_C(\mathbf{r}) - 1 = 0. \tag{19}$$

which are solved simultaneously.

Invoking the factorization of the single chain path integrals, the volume fractions of eq 13−15 expressed in terms of the forward and backward propagators $q(\mathbf{r}, s)$ and $q^{\dagger}(\mathbf{r}, s)$.[26] They are,

$$\varphi_A = \int_{s_0=0}^{s_1} \mathrm{d}s \, \gamma_A(s) q(\mathbf{r}, s) q^{\dagger}(\mathbf{r}, 1-s) \tag{20}$$

$$\varphi_B = \int_{s0}^{s1} \mathrm{d}s \, (1-\gamma_A(s)) q(\mathbf{r}, s) q \dagger (\mathbf{r}, 1-s) + 2\int_{s_1}^{s_2} \mathrm{d}s \, q(\mathbf{r}, s) q^{\dagger}(\mathbf{r}, 1-s) + 4\int_{s_2}^{s_3=1} \mathrm{d}s \, \gamma_B(s) q(\mathbf{r}, s) q^{\dagger}(\mathbf{r}, 1-s) \tag{21}$$

$$\varphi_C = 4\int_{s_2}^{s_3=1} \mathrm{d}s \, (1-\gamma_B(s)) q(\mathbf{r}, s) q^{\dagger}(\mathbf{r}, 1-s) \tag{22}$$

where $q(\mathbf{r}, s)$ is a *forward propagator* which satisfies the same diffusion equation (eq 9) and initial condition ($q(\mathbf{r}, s_0 = 0) = 1$) as the backward propagator. It has the following branching point conditions:

$$q(\mathbf{r}, s_1^R) = q(\mathbf{r}, s_1^L) q^{\dagger}(\mathbf{r}, 1 - s_1^R) \text{ and } q(\mathbf{r}, s_2^R) = q(\mathbf{r}, s_2^L) q^{\dagger}(\mathbf{r}, 1 - s_2^R). \tag{23}$$

We employ a numerical solution of the SCFT equations (eq 13−19) to evaluate the canonical ensemble free energies for various candidate inhomogeneous phases in their unit cells. Initial field configurations are seeded in order to produce a unit cell of a given mesophase, and the modified diffusion equation (eq 9) is solved pseudospectrally with an operator splitting scheme.[38] Using the calculated propagators, the volume fractions and single-molecule partition functions are evaluated. The W_A, W_B, W_C, and P fields are subsequently relaxed using various convergence schemes[26,39,40] in order to satisfy the remaining SCFT equations, (eqs 16−19). We also minimize the free energy density with respect to the volume and shape of the periodic simulation box with a variable cell shape method.[26,41] This optimization determines the cell volume and shape for which there is no residual internal stress. The minor modifications needed to implement these methods in the canonical ensemble are discussed in the Appendix II.

II. The Variable Cell Shape Method. The variable cell shape method,[41] adopted here in the canonical ensemble, involves the minimization of an *intensive* energy density with respect to the size and shape of a unit cell while maintaining a constant segment density.[26] Following the references,[26,41] a cell shape tensor $\mathbf{h}$ is introduced whose components are the three vectors that define the edges of a parallelepiped simulation box. The box shape is relaxed by the following fictitious dynamics scheme:

$$\frac{\mathrm{d}}{\mathrm{d}t}\mathbf{h} = -\lambda_h \mathbf{h}(\Sigma[W_A, W_B, W_C, \mathbf{g}]) \tag{24}$$

where $\mathbf{g}$ is a metric tensor defined as $\mathbf{g} \equiv \mathbf{h}^T\mathbf{h}$ and λ_h is a relaxation parameter. The internal stress produced by the pitchfork-like copolymer molecules is denoted by $\mathbf{\Sigma}$. These internal stresses vanish at equilibrium and can be evaluated in terms of propagators in the canonical ensemble by invoking a factorization of the single chain path integrals:[26,41]

$$\sum[\mathbf{W}, \mathbf{g}] = \frac{2nR_{go}{}^2}{\beta V Q} \sum_{i=0}^{2} \xi_i \times \int \mathrm{d}\mathbf{X} \int_{s_i}^{s_{i+1}} \mathrm{d}s \, q(\mathbf{X}, s) \mathbf{g}^{-1} \nabla \mathbf{x} \nabla \mathbf{x} \, \mathbf{g}^{-1} q^{\dagger}(\mathbf{X}, s-1) \tag{25}$$

In these expressions, ξ_i is the number of identical blocks between the chain positions s_i and s_{i+1} in the copolymer: $\xi_i = \{1, 2, 4\}$. A position vector, $\mathbf{X} = \mathbf{h}^{-1} \cdot \mathbf{r}$, is a cell-scaled position vector whose components lie in [0,1] and $\mathbf{W}$ represents a vector field that is composed of W_A, W_B, and W_C fields.

References and Notes

(1) Naito, K.; Hieda, H.; Sakurai, M.; Kamata, Y.; Asakawa, K. *IEEE Trans. Magn.* **2002**, 51.
(2) Black, C. T.; Ruiz, R.; Breyta, G.; Cheng, J. Y.; Colburn, M. E.; Guarini, K. W.; Kim, H.-C.; Zhang, Y. *IBM J. Res. Dev.* **2007**, *51*, 605.
(3) Lopes, W. A.; Jaeger, H. M. *Nature* **2001**, *414*, 735.
(4) Shimoda, T.; Morii, K.; Seki, S.; Kiguchi, H. *Mater. Res. Soc. Bull.* **2003**, *28*, 821.
(5) Stein, G. E.; Kramer, E. J.; Li, X.; Wang, J. *Phys. Rev. Lett.* **2007**, *98*, 086101.
(6) Bosse, A. W.; Garcia-Cervera, C. J.; Fredrickson, G. H. *Macromolecules* **2007**, *40*, 9570.
(7) Khandpur, A. K.; Farster, S.; Bates, F. S.; Hamley, I. W.; Ryan, A. J.; Brass, W.; Almdal, K.; Mortensen, K. *Macromolecules* **1995**, *28*, 8796.
(8) Matsen, M. W.; Schick, M. *Phys. Rev. Lett.* **1994**, *72*, 2660–2663.
(9) Cochran, E. W.; Garcia-Cervera, C. J.; Fredrickson, G. H. *Macromolecules* **2006**, *39*, 2449.

(10) Cochran, E. W.; Garcia-Cervera, C. J.; Fredrickson, G. H. [Erratum]. *Macromolecules* **2006**, *39*, 4264.
(11) Bang, J.; Kim, S. H.; Drockenmuller, E.; Misner, M. J.; Russell, T. P.; Hawker, C. J. *J. Am. Chem. Soc.* **2006**, *128*, 7622–7629.
(12) Tang, C.; Lennon, E. M.; Fredrickson, G. H.; Kramer, E. J.; Hawker, C. J. *Science* **2008**, *322*, 429–432.
(13) Ko1lbel, M.; Beyersdorff, T.; Cheng, X. H.; Tschierske, C.; Kain, J.; Diele, S. *J. Am. Chem. Soc.* **2001**, *123*, 6809.
(14) Cheng, X.; Prehm, M.; Das, M. K.; Kain, J.; Baumeister, U.; Diele, S.; Leine, D.; Blume, A.; Tschierske, C. *J. Am. Chem. Soc.* **2003**, *125*, 10977.
(15) Chen, B.; Zeng, X.; Baumeister, U.; Ungar, G.; Tschierske, C. *Science* **2005**, *307*, 96.
(16) Liu, F.; Chen, B.; Baumeister, U.; Zeng, X.; Ungar, G.; Tschierske, C. *J. Am. Chem. Soc.* **2007**, *129*, 9578.
(17) Martin-Rapun, R.; Marcos, M.; Omenat, A.; Barbera, J.; Romero, P.; Serrano, J. L. *J. Am. Chem. Soc.* **2005**, *127*, 7397.
(18) Marcos, M.; Martin-Rapun, R.; Omenat, A.; Barbera, J.; Serrano, J. L. *Chem. Mater.* **2006**, *18*, 1206.
(19) Cook, A. G.; Baumeister, U.; Tschierske, C. *J. Mater. Chem.* **2005**, *15*, 1708.
(20) Lenoble, J.; Campidelli, S.; Maringa, N.; Donnio, B.; Guillon, D.; Yevlampieva, N.; Deschenaux, R. *J. Am. Chem. Soc.* **2007**, *129*, 9941.
(21) Zeng, X.; Ungar, G.; Liu, Y.; Percec, V.; Dulcey, A. E.; Hobbs, J. K. *Nature* **2004**, *428*, 157.
(22) Canilho, N.; Kasëmi, E.; Mezzenga, R.; Schlüter, A. D. *J. Am. Chem. Soc.* **2006**, *128*, 13998–13999.
(23) Canilho, N.; Kasëmi, E.; Schlüter, A. D.; Mezzenga, R. *Macromolecules* **2007**, *40*, 2822.
(24) Canilho, N.; Kasëmi, E.; Schlüter, A. D.; Ruokolainen, J.; Mezzenga, R. *Macromolecules* **2007**, *40*, 7609.
(25) Canilho, N.; Kasëmi, E.; Schlüter, A. D.; Ruokolainen, J.; Mezzenga, R. *Macrom. Symp.* **2008**, *270*, 58–64.
(26) Fredrickson, G. H. *The equilibrium theory of inhomogeneous polymers*; Oxford University Press: Oxford, U.K., 2006.
(27) Lindahl, E.; Edholm, O. *Biophys. J.* **2000**, *79*, 426–433.
(28) Marrink, S.; Mark, A. *J. Phys. Chem. B* **2001**, *105*, 6122–6127.
(29) Grason, G. M.; DiDonna, B. A.; Kamien, R. D. *Phys. Rev. Lett.* **2003**, *91*, 058304.
(30) Grason, G. M.; Kamien, R. D. *Phys. Rev. E* **2005**, *71*, 051801.
(31) Hong, K. M.; Noolandi, J. *Macromolecules* **1981**, *14*, 727–736.
(32) Cho, B. K.; Jain, A.; Gruner, S. M.; Wiesner, U. *Science* **2004**, *305*, 1598.
(33) Gido, S. P.; Wang, Z. G. *Macromolecules* **1997**, *30*, 6771.
(34) Matsen, M. W. *J. Chem. Phys.* **1998**, *108*, 785.
(35) Fredrickson, G. H.; Helfand, E. *J. Chem. Phys.* **1987**, *87*, 697.
(36) Lennon, E. M.; Mohler, G. O.; Ceniceros, H. D.; Garcia-Cervera, C. J.; Fredrickson, G. H. *Multiscale Model. Simul.* **2008**, *6*, 1347.
(37) Fredrickson, G. H.; Ganesan, V.; Drolet, F. *Macromolecules* **2002**, *35*, 16–39.
(38) Tzeremes, G.; Rasmussen, K. O.; Lookman, T.; Saxena, A. *Phys. Rev. E* **2002**, *65*, 041806.
(39) Sides, S. W.; Fredrickson, G. H. *Polymer* **2003**, *44*, 5859.
(40) Ceniceros, H. D.; Fredrickson, G. H. *Multiscale Model. Simul.* **2004**, *2*, 452–474.
(41) Barrat, J. L.; Fredrickson, G. H.; Sides, S. W. *J. Phys. Chem. B* **2005**, *109*, 6694–6700.